Technical University of Denmark

DTU

Optical frequency standard using acetylene-filled hollow-core photonic crystal fibers

Triches, Marco; Michieletto, Mattia; Hald, Jan; Lyngsø, Jens Kristian; Lægsgaard, Jesper; Bang, Ole

[Link back to DTU Orbit](#)

DTU Library
Technical Information Center of Denmark

Optical frequency standard using acetylene-filled hollow-core photonic crystal fibers

Marco Triches,[1,2,][*] **Mattia Michieletto,**[2,3] **Jan Hald,**[1] **Jens K. Lyngsø,**[3] **Jesper Lægsgaard,**[2] **and Ole Bang**[2]

[1] *Danish Fundamental Metrology, Matematiktorvet 307, 2800 Kgs. Lyngby, Denmark*
[2] *DTU Fotonik, Department of Photonics Engineering, Technical University of Denmark, Ørsteds Plads 343, 2800 Kgs. Lyngby, Denmark*
[3] *NKT Photonics A/S - Blokken 84, 3460 Birkerød, Denmark*
[*] *mt@dfm.dk*

Abstract: Gas-filled hollow-core photonic crystal fibers are used to stabilize a fiber laser to the $^{13}C_2H_2$ P(16) ($\nu_1 + \nu_3$) transition at 1542 nm using saturated absorption. Four hollow-core fibers with different crystal structure are compared in terms of long term lock-point repeatability and fractional frequency instability. The locked fiber laser shows a fractional frequency instability below 4×10^{-12} for averaging time up to 10^4 s. The lock-point repeatability over more than 1 year is 1.3×10^{-11}, corresponding to a standard deviation of 2.5 kHz. A complete experimental investigation of the light-matter interaction between the spatial modes excited in the fibers and the frequency of the locked laser is presented. A simple theoretical model that explains the interaction is also developed.

© 2015 Optical Society of America

References and links

1. R. Felder, "Practical realization of the definition of the metre, including recommended radiations of other optical frequency standards (2003)," Metrologia **42**, 323–325 (2005).
2. M. de Labachelerie, K. Nakagawa, and M. Ohtsu, "Ultranarrow $^{13}C_2H_2$ saturated-absorption lines at 1.5 μm," Opt. Lett. **19**, 840–842 (1994).
3. J. L. Hall, "Optical heterodyne saturation spectroscopy," Appl. Phys. Lett. **39**, 680–682 (1981).
4. C. Chardonnet, F. Guernet, G. Charton, and C. J. Bordé, "Ultrahigh-resolution saturation spectroscopy using slow molecules in an external cell," Appl. Phys. B: Lasers Opt. **59**, 333–343 (1994).
5. C. Edwards, G. Barwood, P. Gill, and W. Rowley, "Development of acetylene-stabilized diode laser frequency standards," in "15th Annu. Meet. IEEE Lasers Electro-Optics Soc.", (IEEE, 2002), vol. 1, pp. 281–282.
6. A. Czajkowski, A. A. Madej, and P. Dubé, "Development and study of a 1.5 μm optical frequency standard referenced to the P(16) saturated absorption line in the ($\nu 1 + \nu 3$) overtone band of $^{13}C_2H_2$," Opt. Commun. **234**, 259–268 (2004).
7. J. Hald, L. Nielsen, J. C. Petersen, P. Varming, and J. E. Pedersen, "Fiber laser optical frequency standard at 1.54 μm," Opt. Express **19**, 2052–2063 (2011).
8. R. F. Cregan, B. Mangan, P. Russell, J. Knight, P. Roberts, and D. Allan, "Single-mode photonic band gap guidance of light in air," Science **285**, 1537–1539 (1999).
9. F. Benabid, F. Couny, J. C. Knight, T. a. Birks, and P. S. J. Russell, "Compact, stable and efficient all-fibre gas cells using hollow-core photonic crystal fibres," Nature **434**, 488–491 (2005).
10. J. Henningsen, J. Hald, and J. C. Peterson, "Saturated absorption in acetylene and hydrogen cyanide in hollow-core photonic bandgap fibers," Opt. Express **13**, 10475–10482 (2005).

11. R. Thapa, K. Knabe, M. Faheem, A. Naweed, O. L. Weaver, and K. L. Corwin, "Saturated absorption spectroscopy of acetylene gas inside large-core photonic bandgap fiber," Opt. Lett. **31**, 2489–2491 (2006).
12. K. Knabe, S. Wu, J. Lim, K. a. Tillman, P. S. Light, F. Couny, N. Wheeler, R. Thapa, A. M. Jones, J. W. Nicholson, B. R. Washburn, F. Benabid, and K. L. Corwin, "10 kHz accuracy of an optical frequency reference based on $^{12}C_2H_2$-filled large-core kagome photonic crystal fibers," Opt. Express **17**, 16017–16026 (2009).
13. P. T. Marty, J. Morel, and T. Feurer, "All-fiber multi-purpose gas cells and their applications in spectroscopy," J. Light. Technol. **28**, 1236–1240 (2010).
14. J. Henningsen and J. Hald, "Dynamics of gas flow in hollow core photonic bandgap fibers," Appl. Opt. **47**, 2790–2797 (2008).
15. C. Wang, N. V. Wheeler, C. Fourcade-Dutin, M. Grogan, T. D. Bradley, B. R. Washburn, F. Benabid, and K. L. Corwin, "Acetylene frequency references in gas-filled hollow optical fiber and photonic microcells," Appl. Opt. **52**, 5430–5439 (2013).
16. C. Wang, N. V. Wheeler, J. Lim, K. Knabe, M. Grogan, Y. Wang, B. R. Washburn, F. Benabid, and K. L. Corwin, "Portable acetylene frequency references inside sealed hollow-core kagome photonic crystal fiber," in "CLEO2011 - Laser Appl. to Photonic Appl.", (OSA, 2011), p. CFC1.
17. P. J. Roberts, D. P. Williams, H. Sabert, B. J. Mangan, D. M. Bird, T. A. Birks, J. C. Knight, and P. S. J. Russell, "Design of low-loss and highly birefringent hollow-core photonic crystal fiber," Opt. Express **14**, 7329–7341 (2006).
18. R. M. Gerosa, D. H. Spadoti, L. d. S. Menezes, and C. J. S. de Matos, "In-fiber modal Mach-Zehnder interferometer based on the locally post-processed core of a photonic crystal fiber," Opt. Express **19**, 3124–3129 (2011).
19. M. Kusaba and J. Henningsen, "The v_1+v_3 and the $v_1+v_2+v_4^1+v_5^{-1}$ combination bands of $^{13}C_2H_2$. linestrengths, broadening parameters, and pressure shifts," J. Mol. Spectrosc. **209**, 216–227 (2001).
20. V. S. Letokhov, *High-Resolution Laser Spectroscopy*, vol. 13 of *Topics in Applied Physics* (Springer, 1976).
21. J. Hald, J. C. Petersen, and J. Henningsen, "Saturated optical absorption by slow molecules in hollow-core photonic band-gap fibers," Phys. Rev. Lett. **98**, 213902 (2007).
22. V. Dangui, H. K. Kim, M. J. F. Digonnet, and G. S. Kino, "Phase sensitivity to temperature of the fundamental mode in air-guiding photonic-bandgap fibers," Opt. Express **13**, 6669–6684 (2005).
23. D. Payne, A. Barlow, and J. Ramskov Hansen, "Development of low- and high-birefringence optical fibers," IEEE Trans. Microwave Theory Tech. **30**, 323–334 (1982).
24. I. Kaminow, "Polarization in optical fibers," IEEE J. Quantum Electron. **17**, 15–22 (1981).
25. W. Demtröder, *Laser Spectroscopy: Basic Concepts and Instrumentation* (Springer, 1996).
26. J. M. Fini, J. W. Nicholson, B. Mangan, L. Meng, R. S. Windeler, E. M. Monberg, A. DeSantolo, F. V. DiMarcello, and K. Mukasa, "Polarization maintaining single-mode low-loss hollow-core fibres," Nat. Commun. **5**, 5085 (2014).
27. M. Michieletto, J. K. Lyngsø, J. Lægsgaard, and O. Bang, "Cladding defects in hollow core fibers for surface mode suppression and improved birefringence," Opt. Express **22**, 23324–23332 (2014).
28. E. N. Fokoua, M. N. Petrovich, N. K. Baddela, N. V. Wheeler, J. R. Hayes, F. Poletti, and D. J. Richardson, "Real-time prediction of structural and optical properties of hollow-core photonic bandgap fibers during fabrication," Opt. Lett. **38**, 1382–1384 (2013).
29. J. K. Lyngsø, C. Jakobsen, H. R. Simonsen, and J. Broeng, "Single-mode 7-cell core hollow core photonics crystal fiber with increased bandwidth," Proc. SPIE in "21st Int. Conf. Opt. Fibre Sensors," **7753**, 77533Q (International Society for Optics and Photonics, 2011).
30. J. L. Hall and C. J. Borde, "Shift and broadening of saturated absorption resonances due to curvature of the laser wave fronts," Appl. Phys. Lett. **29**, 788–790 (1976).
31. S. E. Park, H. S. Lee, T. Y. Kwon, and H. Cho, "Dispersion-like signals in velocity-selective saturated-absorption spectroscopy," Opt. Commun. **192**, 49–55 (2001).

1. Introduction

Portable optical frequency standards are important in metrology and in many other applications (optical sensing, telecommunication, aerospace, etc.) that need an accurate and reliable optical reference away from the laboratories. In the telecommunication band the $^{13}C_2H_2$ P(16) ($v_1 + v_3$) line at 1542.3837 nm is the recommended optical transition for the realization of the meter [1]. During the last decade, I_2, acetylene and Rb vapour cells have been widely investigated and implemented in laser stabilization using the saturated absorption spectroscopy (SAS) technique [2], often combined with frequency modulated spectroscopy [3–7]. Since the demonstration of the first photonic band gap guidance in air [8], the increased availability of fibers with an hollow core (HC) allowed to investigate the realization of a *portable*

optical frequency reference based on a gas-filled HC fiber [9–13].

Hollow core fibers are particularly useful in this technology because they provide a very long interaction length in a compact space. Moreover, the possibility to develop an all fiber-based optical reference makes this solution easier to implement in an industrial environment. However, developing a portable and user-friendly optical frequency standard is not free of challenges; although fiber gas-filling and other main technical issues have already been characterized [14], targeting the most suitable fiber for this technology is still under debate. State of the art research suggest that kagome fibers produce better performance than more common hollow core photonic crystal fibers (HC-PCF), both in terms of lock-point repeatability and stability [12, 15]. Limited transit-time broadening due to larger core size and absence of surface modes are the key-features of the kagome fibers. On the other hand, they are highly multi-mode, which could create an issue for long term frequency stability, as mentioned in [12].

SAS technique used to frequency-lock lasers to a sub-Doppler optical transition is limited by the strength of the signal and the linewidth of the sub-Doppler feature. Maximizing the strength of the signal while choosing a narrow-linewidth transition is the target of any frequency locking scheme. As shown in previous work [10], the major contribution to the width of a sub-Doppler absorption line in HC fibers is due to the transit-time broadening effect. Therefore, having a larger core diameter seems to be the best solution to reduce the instability.

Despite the previous considerations, the multi-mode characteristic of the large core kagome fibers could introduce a factor of instability, mainly related to the lock-point repeatability. Previously published works ascribe this effect to the presence of high order modes (HOMs) [12], surface modes [15] inside the *band gap* or polarization instability between the pump and probe beams [16]. The mechanism ascribed to the lock-point inaccuracy presented in [12] suffers a lack of universality and it cannot explain some of the effects presented in these paper. This work aims at demonstrating that most of these effects are directly connected to the interaction between different spatial modes inside the fiber. The correlation between the modes excited in the HC fibers and the repeatability of the lock-point is investigated and a simple theoretical approach is proposed to explain the physical mechanism involved.
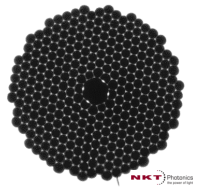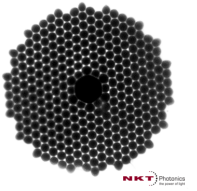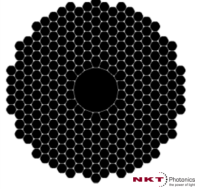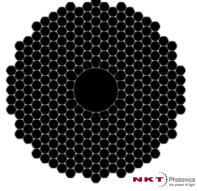
Here we present a complete characterization of four different HC-PCFs, investigating their performances, using SAS combined with a frequency modulation spectroscopy technique. The performance achieved improves previously published results [12, 15] for gas-filled HC fibers both in terms of frequency stability and lock-point repeatability, reducing the gap with respect to the performance achieved with bulk glass cells [7].

2. Fiber characterization

2.1. Fiber specifications overview

Before testing the fibers in the SAS setup, a detailed investigation on the HOM contents of the various HC fibers is needed to check any (possible) correlation between the HOMs guided and the stabilization performance. In this section we compare the fiber characteristics with the HOMs investigation. The relevant properties of the HC fibers are listed in Table 1. Three fibers have a 7-cell core whereas the last one is a 19-cell HC fiber. The C7‗ PM fiber differs from all the others as it is fabricated to be polarization maintaining (PM). The enhanced birefringence needed to have the PM property is introduced thanks to four anti-resonant features on the core wall [17]. At the same time, these features lead to improved mode confinement. The C7‗ L and C7‗ S fiber have about the same crystal structure, but with different scaling factor (*pitch*), which results in a larger core size of C7‗ L with respect to C7‗ S. To simplify the notation, in the rest of the manuscript we will refer to the different fibers as *single* mode, *few* mode or *multi* mode fiber with respect to the mode content at 1542 nm. All the fibers tested have a total loss lower than 18 dB/Km at the addressed wavelength and they are provided by NKT Photonics.

Table 1. Summary of the fiber characteristics.

Specs/Name	C7_PM	C7_L	C7_S	C19
Core	7-cell	7-cell	7-cell	19-cell
Core diameter	9.3 μm	11.9 μm	8.5 μm	20.0 μm
MFD	6.8 μm	8.2 μm	5.4 μm	13.2 μm
Coupling	63%	67%	61%	72%
PM property	PM	non-PM	non-PM	non-PM
Modes property	single-mode	*few*-mode	single-mode	multi-mode
Structure				

2.2. HOMs characterization: in-fiber Mach-Zender interferometer

The HOM characterization is performed using a setup similar to the one presented in [18]. A super-continuum source (0.45-2.4 μm) is coupled to a piece of 8 cm of HC fiber and is collected with a single-mode (SM) fiber into an optical spectrum analyzer (OSA). Each spectrum is recorded across most of the fiber band gap with 0.1 nm resolution. The total field distribution and hence the coupling efficiency to the SM fiber depends on the relative phase of the modes. The different spatial modes excited in the HC fiber are interfering once collected into the SM fiber, due to their different group velocity. The configuration is similar to a Mach-Zender interferometer, where the reference arm is provided by the light in the fundamental mode (FM). The difference between the group velocity of the FM and the one of a given HOM/surface mode gives rise to a wavelength dependent phase difference. The spectrum is then processed applying a windowed Fourier transform (WFT) analysis, which highlights the HOMs excited in terms of the group velocity refractive index difference (Δn_g) with respect to the FM ($\Delta n_g = 0$). The results are presented in Fig. 1. The *flat* feature visible at $\Delta n_g \simeq 0.08$ that affects most of the spectrum is an artifact introduced by the apparatus. In fact, it does not depend on the fiber tested because it is reproduced in all the tests performed at the same effective group index difference. Except from this artifact, the fibers show widely different features. The C7_PM has a strong feature with $\Delta n_g \leq 0.05$, which covers most of the spectrum and strongly diverges around 1650 nm: this is probably due to an anti-crossing between the FM and a surface mode. Despite the measurement here presented could not resolve it, the fiber guides two orthogonal polarized FMs with two different effective refractive index (and/or different group velocity refractive index), due to its enhanced birefringence. The C19 fiber is clearly showing a multi-mode behavior.

The most interesting features are related to the C7_L and the C7_S. Even though they have a similar photonic crystal structure, the larger core of the C7_L fiber allows *few* HOMs to be guided at 1542 nm, with propagation constant close to the FM, which are absent in the C7_S spectrum. Moreover, a strong beating at a higher group index difference ($\Delta n_g \approx 0.15$) suggests the presence of a *surface* mode (localized on the core-wall). These considerations will be more clear in Section 5.1, where the C7_L spectrum acquired will be compared with simulations.

The HOM excitation in the HC fibers is also strongly influenced by the coupling. In order to characterize the coupling dependence of the spectra observed, the measurements are repeated with a (strongly) misaligned in-coupling beam: the misalignment increases the light intensity coupled to the various HOM components, but does not give rise to any HOMs different than
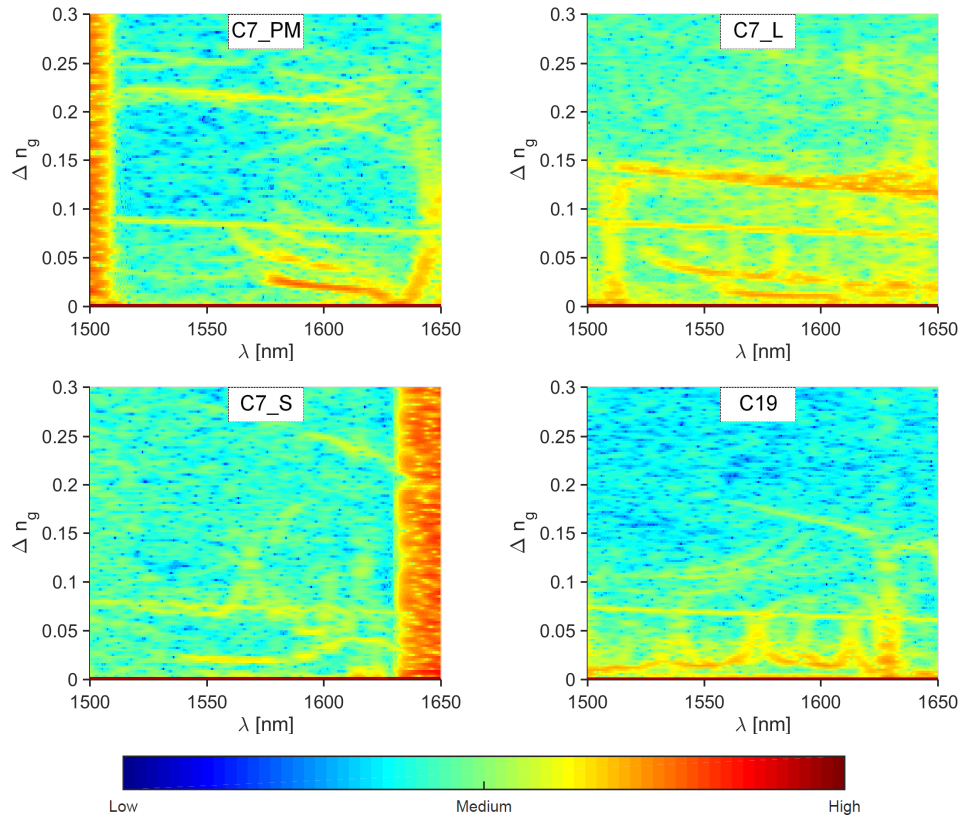
Fig. 1. WFT analysis of the spectra collected. The HOMs/surface modes are represented by the *yellow/orange* features. The the *red* border represent the band gap edge/cladding modes (C7_ S). The "flat" yellow feature present in all the measurements ($\Delta n_g \approx 0.08$) is an artifact introduced by the setup. The colors represent the light intensity, according to the legend [a.u.].

the ones previously observed. This test also simulates the effect of possible deviations from optimal coupling that might occur in the SAS setup. The investigations in [12] suggest that the presence of the HOMs/surfaces mode in similar setup could shift the frequency of the locked laser by few MHz, but an high number of HOMs should average out the effect, reducing the overall shift observed (on the order of few kHz). Moreover, the presence of some surface modes could enhance the light coupling to the HOMs, changing the mode field distribution of the core-guided modes [15]. Following these interpretations, the highly multi-mode fiber (C19) should produce a limited shift of a few kHz, while no shift of the locked laser frequency is expected if no HOMs are excited (C7_ S fiber). On the contrary, the shift should be stronger (a few MHz) if only a *few* HOMs are excited at the operational wavelength (C7_ L fiber), because the averaging mechanism does not occur to reduce overall shift. As the following analysis will clarify, some of these assumptions appear incorrect.

3. Experimental SAS setup

A SAS setup similar to the one described in [3] is used to investigate the four different HC fibers (Fig. 2). A sealed box with AR coated windows is connected to a vacuum pump and to

an acetylene vessel. A fiber laser source (Koheras E15 Adjustik$^{\text{TM}}$) of 30 mW power is split into two beams, and coupled into the HC fiber placed inside the box with free-space optics.
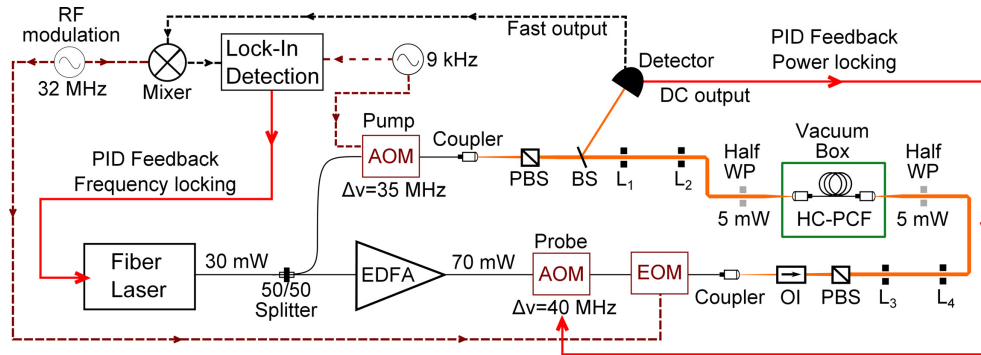

Fig. 2. Schematic layout of the SAS Setup. OI: optical isolator. (P)BS: (polarized) beam splitter. L_{1-4}: lenses. Half WP: half wave plate.

Using an acousto-optic modulator (AOM) the light of the first beam (called *pump*) is intensity modulated at 9 kHz using an external square-wave function generator, and blue-detuned by 35 MHz. The other (*probe*) beam is blue-detuned by 40 MHz using a second AOM, after being amplified by an erbium-doped fiber amplifier (EDFA). This configuration avoids low-frequency noise ($\leq$100 kHz) from the interference between the two counter-propagating beams, while it maintains the sub-Doppler feature in the central part of the Doppler absorption profile, where the signal-to-noise ratio is high.

The probe is also phase modulated through an electro-optic modulator (EOM) at 32 MHz to generate the side-bands needed for frequency modulation spectroscopy. The transmitted probe beam is detected using a beam splitter and free space coupling to a low noise detector, with both AC and DC response. The fast signal is used to lock the laser to the optical transition, using a lock-in amplifier combined with a servo-loop. The same square function used to modulate the pump intensity is providing the detection reference. Meanwhile, the DC output is used to stabilize the probe power via the probe AOM. Both beams have a power of 5.5 mW at the HC-fiber input; since the saturation power (P_{sat}) measured in similar system is more than 20 mW [10], the experiment presented here is in the low saturation regime ($P \ll P_{\text{sat}}$). A small fraction of the laser output is combined with the output of a reference laser and the resulting beat signal is monitored with a fast photodiode and a frequency counter. The reference laser is locked to an an acetylene bulk glass cell as described in [7] and it has a frequency instability (Allan deviation) below 5×10^{-13} for sampling time $1 < \tau < 10^5$ s and a lock-point repeatability of about 100 Hz.

The box is temperature controlled through a Peltier cell deployed underneath and the temperature inside the box is monitored using two Pt-100 probes. This configuration allows testing the fibers both in a stable and varying temperature environment, in order to investigate how fiber temperature affects the frequency stability. The polarization of the two counter propagating beams is controlled using a polarized beam splitter (PBS) combined with zero-order half wave plates. The fiber is placed inside the chamber, coiled with a diameter of about 6 cm. Once cleaved, both the facets are connected to a free space coupler fixed inside the chamber, using bare fiber adapters. Each fiber is left under vacuum ($\leq 3 \times 10^{-6}$ hPa) for about a week.

After the purging step, the chamber is exposed to 29 Pa of $^{13}\text{C}_2\text{H}_2$ vapour. All the fibers tested are about 3 m. The filling pressure and the length of the fibers have been chosen to limit the filling time (less than 30 min) and the pressure broadening. Therefore, the contribution to

the full with half maximum (FWHM) of the transition profile due to the gas pressure is limited to 6 MHz [7], while the calculated absorption of the $^{13}C_2H_2$ P(16) line for a 3 m fiber at 29 Pa is about 54% [19]. As previously mentioned, the transit-time broadening is the major limiting factor for SAS in HC fibers, because the mode field diameter (MFD) is one order of magnitude smaller than what is typically used in bulk vapour cell systems. This effect is inversely proportional to the MFD and the FWHM contribution is about 15 to 30 MHz, depending on the fiber tested [20, 21].

4.   Performance evaluation

The fiber test takes about 30 hours and it is subdivided in three consecutive phases. In the first phase the temperature of the is box stabilized to 24°C (12 hours) while a temperature variation is induced during the second phase (12 hours, see Section 4.2). During the third phase, the temperature is restored to the initial condition and the fiber is tested to check that performance is consistent with the one observed in the first phase. The last phase takes about 6 hours and it is important to check that the temperature ramp does not introduce any permanent effects in the setup/fiber due to thermal expansion of some components inside the box (fiber holder, free space couplers etc). All the measurements presented show comparable performance between the first and third phase. The measurements are also repeated after each fiber is re-cleaved/re-filled to check the reproducibility of the results, presenting comparable performance. The second phase is done to check the temperature sensitivity and to simulate the the long term performance of the fiber. The temperature variation has been previously investigated as a source of phase instability in fiber optic gyroscope (FOG) applications [22], arising from the differential thermal expansion between the spool and the glass, and the instability observed is stronger if the fiber is birefringent. The birefringence could be due to a deformed/elliptical core [23] or because of the anti-resonant elements introduced in the core wall (C7₋ PM). Moreover, the temperature stress induces small mechanical variations in the components inside the box (coupler/holder), simulating coupling changes that could occur on the long term scale (days). The frequency difference between the laser locked to the gas-filled HC fibers and the reference laser are presented in Fig. 3 and 4 together with the corresponding fractional frequency instability (Allan deviation). The frequency offset results are plotted with a relative shift of 100 kHz for clarity.

4.1.   Temperature stabilized environment

Here we present the results obtained with the four fibers under a temperature stabilized environment (first phase). The difference between the single-mode and the multi-mode fibers is clearly visible (Fig. 3, left). The fluctuations observed are within about 25 kHz for most of the fibers, while the laser locked to fiber C7₋ S shows a remarkable *stability* with an offset limited to 4 kHz. This test confirms that the presence of the multiple modes excited in a fiber contributes to a shift of the laser frequency.

The performance of the C7₋ PM fiber needs a dedicated explanation: although the previous analysis (Fig. 1) does not show the presence of HOMs at 1542 nm, this fiber guides two *orthogonal* polarized modes with a slightly different effective refractive index. In this sense, the interaction between the two orthogonal polarized FMs introduces a perturbation in the light-matter interaction similar to the one given by a FM-HOM one. The interaction mechanism will be discussed in Section 6. Moreover, if the launched polarization is not aligned to one of the major axes, the SAS configuration will not be the one described in Section 3 (two counter propagating beams with orthogonal polarized light). Depending on the *beat length* of the fiber and on the misalignment, the modal content could vary over the interaction length, generating a superposition of linear/elliptical/circular polarized light in both the beams [24]. This non-homogeneous polarization combined with the different propagation constant of the two orthogonal polarized
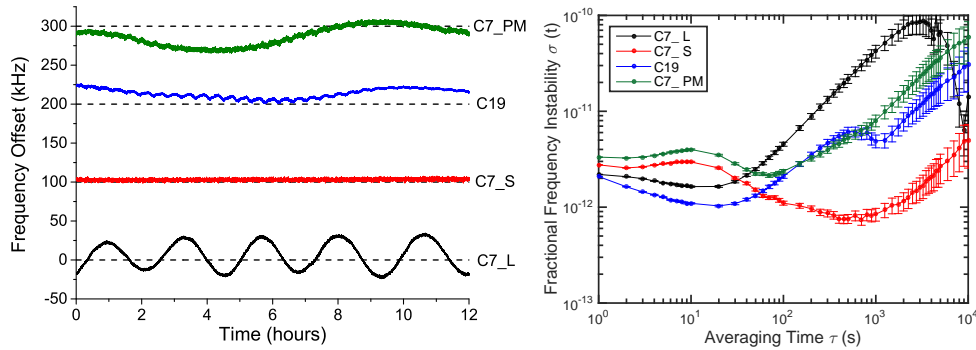
Fig. 3. Stable environment test: Frequency of the locked laser over time (left). The results are plotted with a relative shift of 100 kHz for clarity, after the frequency of the reference laser [7] is subtracted. Fractional frequency instability (*Allan* deviation) of the four fibers (right).

FMs could contribute to the instability observed in Fig. 3. This consideration is supported by the measurements done during the temperature variation (Fig. 4).

The fractional frequency instability is presented in Fig. 3 (right). The long-term performance ($\tau \geq 100$ s) confirms the remarked difference between the C7_S and the other fibers: the *multi-mode* fibers follow the same trend (increased instability), while the C7_S presents an instability below 4×10^{-12} for $1 < \tau < 10^4$ s. In the short term ($\tau < 100$ s), the instability is inversely proportional to the MFD: the noise of the locked-laser depends on the slope of the error signal produced for locking, which is inversely proportional to the linewidth (FWHM) of the transition addressed. The linewidth is dominated by the transit-time broadening caused by the small beam diameter [20,21]. The measured instability confirms this effect within the experimental uncertainties, except for the PM fiber, since the MFD of the C7_PM is larger than the C7_S. The second phase of the test could help to clarify this unexpected performance.

4.2. Environment under temperature variation

The temperature ramp applied is described in Fig. 4 (bottom-right corner). The test under temperature variation confirms the validity of the previous analysis: the amplitude of the fluctuations observed in the *multi-mode* fibers are comparable, while the frequency variations of the C7_S fiber remain within 10 kHz. Despite the slow temperature variation introduced (less than 1.7°C/hour, Fig. 4 bottom-right corner), the perturbation can easily excite HOMs/surface modes, increasing the instability. The test also shows that the lock-point stability is almost temperature insensitive for the C7_S fiber, maintaining the fractional frequency instability well below 1×10^{-11}, giving us the best candidate for a future portable optical frequency standard. Practically, the thermal stress introduced is enhancing the frequency fluctuations previously observed (Fig. 3, left), reducing the timescale of the oscillations by a factor 10. This fact confirms that the introduced stress helps to understand the long-term performance of the various fibers, considerably reducing the total acquisition time. All the measurements show comparable maximum shift in the repeated tests. A detailed analysis of the PM fiber performance in Fig. 4 shows that the fractional frequency instability at 1 s averaging time is increased by a factor 2 with respect to to what observed in the first phase of the test (Fig. 3). This effect occurs only to the PM fiber while the others show comparable instability in all the phases of the test (at 1 s). Moreover, the instability of the C7_PM shown during the third phase of the test reproduces the behavior shown in Fig. 3, excluding that a permanent perturbation has been introduced on the
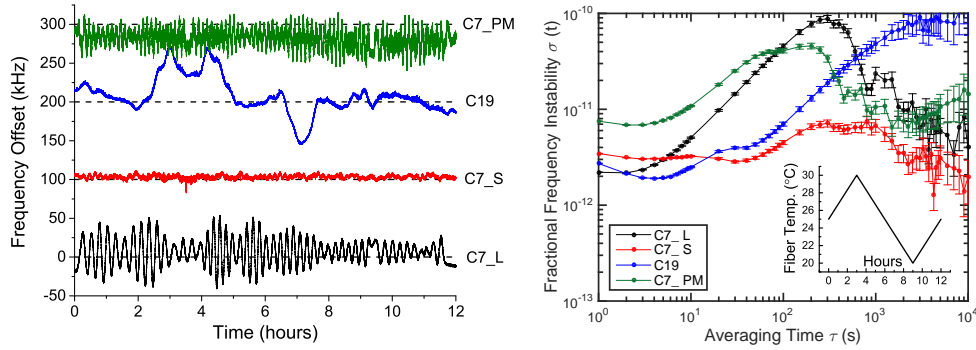
Fig. 4. Stress test. Frequency of the locked laser over time (left). The results are plotted with a relative shift of 100 kHz for clarity, after the frequency of the reference laser [7] is subtracted. Fractional frequency instability (*Allan* deviation) of the four fibers (right). The temperature ramp applied is plotted in the bottom-right corner.

setup/fiber.

This effect could not be ascribed to the HOMs contribution to the light-matter interaction, which can explain the long term oscillations observed ($\tau > 10$ s), as presented in Sec. 6. Following the previous considerations, a possible explanation could come from the polarization instability, since the different light polarization between the pump and probe beam is known to affect Lamb dip detection [25]. The mechanical stress introduced by the temperature ramp could cause small *deformations* in the fiber structure, changing the relative propagation constant between the two orthogonal polarized FMs [22, 23]. An other source of instability could come from the presence of some surface modes introduced by the special core wall structure of this fiber. Since the maximum Δn_g shown in Fig. 1 is limited by the resolution of the OSA, there could be some surface modes at 1542 nm with $\Delta n_g > 0.3$, which are not highlighted by the measurements. The tests performed allow anyway to conclude that the C7‿PM has an enhanced temperature sensitivity with respect to the other fibers. These characteristics possibly make this fiber suitable for sensors applications. Possible candidate PM fiber suitable for this technology can be the fiber recently demonstrated in [26] or in [27]. The *defects* introduced in the cladding structure make these fibers PM without introducing additional surface modes which could affect the FM. In this sense, one of these fiber could also help to discriminate the source of the instability here observed on the C7‿PM.

4.3. Overall comparison

Considering the overall performances, the C7‿S fiber is the most suitable for the frequency standard applications, showing a fractional frequency instability $\leq 8 \times 10^{-12}$ in a *stressed* environment and better performance in a controlled one ($\sigma(\tau) < 4 \times 10^{-12}$, $1 < \tau < 10^4$ s timescale). The C7‿S fiber is also tested over 55 hrs (in a temperature stabilized environment), in order to compare the instability of the system developed here with previously published results. Fig. 5 (left) compares the performance of the C7‿S fiber with the stabilized laser presented in [12] (gas-filled kagome fiber) and with the performance of the reference laser [7]. The lowered instability achieved with respect to [12] is reducing the gap between the bulk cell performance and the HC-fiber based system. The lock-point repeatability is also measured on 6 different days (Fig. 5, right): the system shows an average shift of 3.6 kHz with respect to the reference, with a standard deviation of 2.5 kHz. This analysis of the *long-term* performance shows a consistent result over a period of more than 1 year.
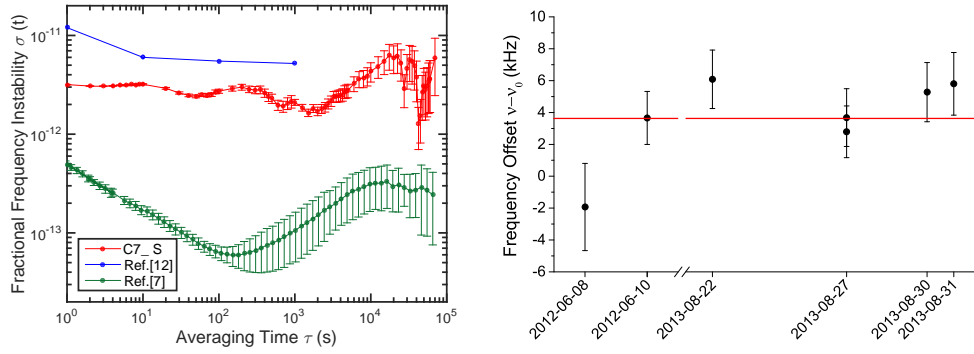
Fig. 5. Left: Summary of the performance achieved using the C7_S fiber in a temperature stabilized environment (red). The system is compared with the reference laser [7] stabilized to a bulk glass cell (green) and with the best performance reported in [12] for an gas-filled HC-fiber stabilized laser (blue). Right: The lock-point repeatability over 7 measurements. The error bars represent the root mean square value of the measured data.

5. Modelling of HOMs

In order to understand how the different modes could influence the frequency of locked laser, a numerical investigation on the mode content is performed. The C7_L fiber has similar properties to that of C7_S, nonetheless the C7_L results in a larger variation of the laser frequency. We believe the reason is the presence of HOMs at the addressed wavelength as highlighted by the measurements in Fig. 1. For this reason fiber C7_L is chosen for the numerical investigation. The purpose of this analysis is to address the mode(s) that could be responsible of the frequency shift/fluctuation observed. The simulations are performed starting from an idealized model of a 7-cell HC-PCF structure, using the parameters measured on the cane during the fiber drawing process, according to [28, 29]. Results are shown in Fig. 6.
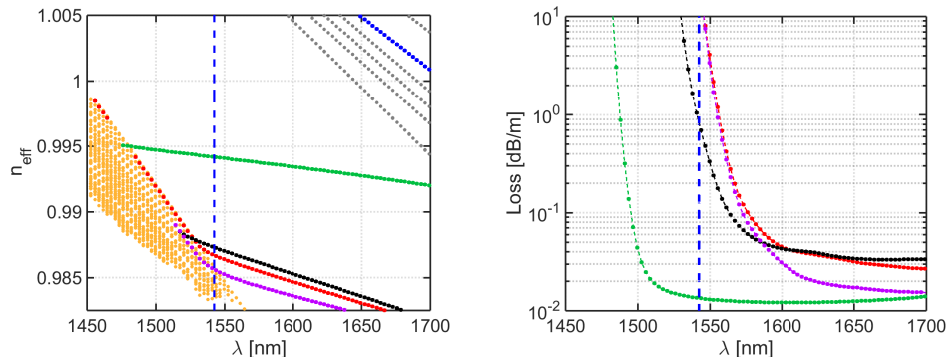

Fig. 6. Simulation results of C7_L. The mode trajectories (left) and the loss of the different modes (right) are plotted. The FM is plotted in green, the cladding modes in orange and the surface modes in grey. Three HOMs (red, violet and black dots) and a surface mode (blue) are highlighted. A dashed blue line at 1542 nm is added. The surface modes on the left figure are omitted for clarity.

The FM and the relevant HOMs/surface modes are highlighted. The loss data plotted is limited to the 10 dB/m for clarity. Remembering that the tested fibers have a length of 3 m, Fig. 6 (right) can also represent the transmission of the different modes through the fiber: 10^{-2} dB/m

corresponds to 99% while 10 dB/m gives 0.1% of transmission. Therefore, the simulations show that only one HOM has a loss low enough to be detected (black curve).

5.1. Simulated and measured spectrum comparison

A direct comparison between simulated and measured spectrum requires the calculation of the group refractive index (n_g) of the simulated modes

$$n_g = n_{\text{eff}} - \lambda \frac{dn_{\text{eff}}}{d\lambda} \tag{1}$$

where λ is the wavelength and n_{eff} is the effective refractive index. The group index difference with respect to the FM (Δn_g) superimposed on the spectrogram of the C7_L fiber from Fig. 1 is presented in Fig. 7. The intensity profiles are also plotted to clarify the difference between the modes.

The simulations reproduce quite well the measured mode content and they confirm that the features with a lower group index difference (less than 0.05) are HOMs excited in the fiber, while the strong feature observed at $\Delta n_g \sim 0.12$ that covers most of the band gap is a surface mode (or a combination of many of those). The simulations also confirm that the flat feature at $\Delta n_g \sim 0.08$ is not caused by any HOM/surface mode. Since the simulation of the surface modes is strongly dependent on the accuracy of the description of the structures surrounding the core wall, the numerical evaluation of the surface modes is less trustworthy than the HOMs one. A deeper investigation (using e.g. SEM/AFM images) is necessary to have a better knowledge of the geometry that surrounds the core, in order to obtain a more reliable simulation of surface modes.
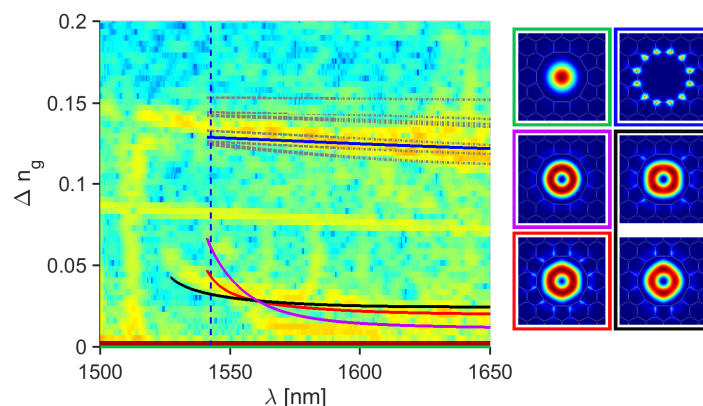

Fig. 7. The group index evaluation of the various modes is compared with the experimental data of the fiber C7_L from Fig. 1 (left). The colors are the same used in Fig. 6. The FM is visible at $\Delta n_g = 0$ (green). The intensity profile of the different modes simulated is plotted (right). The HOM represented in *black* is in fact the superposition of two different modes, as highlighted by the mode intensity profiles on the right.

6. Laser frequency shift: a simple theoretical approach

The frequency shift observed in the multi-mode fibers presented in Fig. 3 needs to be explained. Any change in one of the fundamental parameters that defines the light-matter interaction can (potentially) cause a shift in the lock-point frequency. Wave front curvature [30] and angled

beams interaction [31] are known to cause frequency shift in SAS with bulk vapour cells. However, these effects cannot directly explain frequency shifts when using HC fiber as gas cell. The wave-front curvature in the HC fiber is negligible (plane wave) and the beams are confined along the same propagation path (the counter-propagating k-vectors are aligned).

Temperature effects are already discussed in Section 4. The pressure variation is below 0.5 Pa over the entire test and it has negligible influence. The probe and pump power are monitored along the tests, showing fluctuations of 0.05 mW and 0.3 mW respectively (one standard deviation). The numerical value of the power sensitivity coefficient is measured to be below 15 kHz/mW for both the beams. Therefore, the observed power fluctuations combined with the power sensitivity cannot explain the ± 25 kHz frequency fluctuations observed for the multi-mode fibers. However, a correlation between the the frequency fluctuations for the C7_ PM fiber and spatial mode variations of the probe/pump beam is observed. An infrared camera monitors a small fraction of the probe beam, and the beam shape oscillates about 50 times when the temperature is increased by 5°C. This compares qualitatively to the number of frequency oscillations for a 5°C temperature change as seen in Fig. 4. Similarly, if a small misalignment is introduced so that the output power at the fiber facet changes less than 1%, the mode shape clearly oscillates. These observations suggest that fluctuations in the modal content are responsible for the observed frequency fluctuations.

Previously published work [12] reports a frequency shift in large core kagome fibers (diameter $\sim 60~\mu$m) comparable to the one presented here. According to [12] various spatial modes could cause a shift comparable to the Doppler shift observed in a free space interaction of two angled beams. Although the Doppler effect should give a theoretical shift of few MHz, they argue that the interaction between many HOMs should average out, reducing the final shift to the kHz level. We demonstrate that this explanation is not generally sufficient. Observing Fig. 6 and 7, only one mode has a low enough loss to be taken into account (black curve), but the maximum shift observed for the C7_ L fiber is only ± 50 kHz with respect to the reference [7]. Hence we observe a small shift at the kHz level which cannot be explained by an averaging of many HOM interactions. We aim to present here a simple theoretical model that describes the mechanism involved in the frequency shift for the different types of HC fibers, also in case of a HC fiber that guides *few* modes at the addressed wavelength, like the C7_L considered.

The mechanism is based on the Doppler shift effect, taking into account the intensities associated to the different modes. In order to keep the theoretical model simple, only two modes are considered for the C7_ L fiber: the FM and the HOM with the lower loss (Fig. 6, black). The two counter-propagating beams (pump and probe) can be described as a superposition of the FM and the HOM component. Therefore, the (pump,probe) interaction could be decomposed in four different contributions due to the modal content of each beam: (FM,FM) + (FM,HOM) + (HOM,FM) + (HOM,HOM). Each contribution is treated separately and the single effects are subsequently summed, which is possible as the modes are orthogonal. In general, in order to saturate the molecules, the k-vectors of the two laser beams should fulfill the following expression

$$\mathbf{k_i} \cdot \mathbf{v} = \mathbf{k_j} \cdot \mathbf{v} \qquad (2)$$

where $i = 1, 2$ and $j = 3, 4$ refers to the probe and pump components respectively (as labeled in Fig. 8), while $\mathbf{v}$ is the velocity of the molecules addressed by the two beams.

Since the k-vector component along the propagation axes depends on the effective refractive index of the mode considered, the interaction inside the fiber is the analogue of an angled beam interaction in a vapour bulk cell. Inside the HC fibers, the shift is not caused by a *real* angle between the counter propagating k-vectors, it is given by an *effective angle* that comes from the different propagation constant (β_i) of the modes. The *effective angle* (θ_i) of each mode
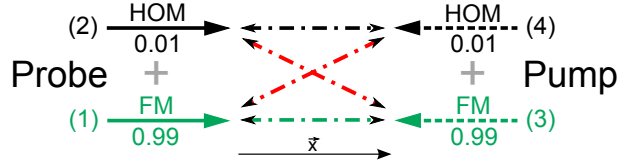
Fig. 8. Schematic representation of the light-matter interaction. The green arrows indicate the FM, the black ones the HOM component. The interactions are depicted with dotted-dashed line in green (FM-FM), red (FM-HOM and HOM-FM) and black (HOM-HOM). The number reported under each mode component refers to the associated normalized light intensity. The components are also enumerated for clarity. The axis orientation chosen is shown.

considered can be defined as follow

$$
\begin{cases} \beta_{\mathbf{i}} = n_{\text{eff}_i} k_0 \hat{\mathbf{x}} \\ \beta_{\mathbf{0}} = n_0 k_0 \hat{\mathbf{x}} \end{cases} \implies \cos\theta_i = \frac{n_{\text{eff}_i}}{n_0} \implies \begin{cases} \theta_{1,3} = 0.11 \\ \theta_{2,4} = 0.16 \end{cases} \tag{3}
$$

where n_0 and k_0 are the refractive index and the wave number in vacuum, and $\beta_i = n_{\text{eff}_i} k_0$ is the propagation constant associated to the different modes. Rewriting the Eq. (2) with the effective angles defined in Eq. (3), the Doppler shift (Δv_{ij}) of the different interaction is given by

$$
k_0 \begin{bmatrix} \cos\theta_i \\ \sin\theta_i \end{bmatrix} \cdot \begin{bmatrix} v_x \\ v_y \end{bmatrix} = k_0 \begin{bmatrix} \cos(\pi+\theta_j) \\ \sin(\pi+\theta_j) \end{bmatrix} \cdot \begin{bmatrix} v_x \\ v_y \end{bmatrix} \implies \Delta v_{ij} = \frac{v}{\lambda_0}\sin\left(\frac{\theta_j - \theta_i}{2}\right) \tag{4}
$$

where the angle π gained by the pump components is due to the fact that the pump is propagating in the opposite direction with respect to the probe (Fig. 8), and $v = \sqrt{v_x^2 + v_y^2}$ is the thermal velocity of the molecules (≈ 435 m/s). Therefore, the contribution to the shift can *only* be due to the interactions between a FM and a HOM component. Moreover, when the $\theta_j > \theta_i$ the center of the sub-Doppler line shape experience a positive shift, while a negative shift occurs if $\theta_j < \theta_i$. This fact gives rise to an opposite contribution from the two FM-HOM interactions: the (2,3) interaction addresses a class of molecules with a velocity component $+v_x$ (same direction of the probe beam, $\beta_2 < \beta_3$), while the (1,4) interaction addresses a class of molecules with a velocity component $-v_x$ (opposite direction, $\beta_1 > \beta_4$). The *theoretical* shift Δv_{ij} given by Eq. (4) is approximately $+7$ and -7 MHz for the (1,4) and (2,3) interactions respectively, and zero otherwise (for the C7_ L fiber considered).

In order to take into account the light intensity of the various interaction, we define f_i as the normalized intensity associated to each mode. The light intensity associated to the each interaction is defined as $I_{ij} = f_i \cdot f_j$, $i = 1, 2$ and $j = 3, 4$, assuming that the pump/probe have the same power at the fiber input. Therefore, the line-shape $I(v)$ of the sub-Doppler absorption line will be the superposition of four interactions

$$
I(v) \propto \sum_{i=1}^{2}\sum_{j=3}^{4} \frac{I_{ij}}{4\pi} \frac{\Gamma_0}{(v - v_0 \pm \Delta v_{ij})^2 + \left(\frac{\Gamma_0}{2}\right)^2} \tag{5}
$$

where Γ_0 and v_0 are the FWHM and the frequency of the sub-Doppler transition addressed. Taking into account the transit-time and the pressure broadening effect, the FWHM for the fiber considered is $\Gamma_0 \approx 26$ MHz [20, 21]. Depending on the I_{ij}, Δv_{ij} and Γ_0, the maximum of the line-shape $I(v)$ could experience a *shift* (Δv_{TOT}). In fact, the *shift* of the maximum of the line-shape $I(v)$ is a distortion of the typical Lorentzian profile caused by the superposition of

four interactions not centered on the same frequency. Therefore, the fact that the shift observed is limited to the kHz level is due to the combination of the symmetry of the pump/probe configuration and the low intensity associated to the HOMs (with respect to the FM one). This *shift* directly affects the laser frequency, because it changes the zero-crossing point of the dispersion-like signal used for locking.

In order to simplify the analysis of the model predictions, we assume the following light intensity of the mode components:

- 1% of light coupled to the HOM component ($f_{2,4} = 0.01$);

- 99% of light coupled to the FM component ($f_{1,3} = 0.99$);

This light intensity configuration is not arbitrary and it could be considered as an upper limit: the WFT analysis on the C7$_-$ L fiber (Fig. 1) shows that the HOM considered (black) has an intensity more than 50 times lower than the FM (after 8 cm of fiber, at 1542 nm) and the HOM considered has 3 dB loss across the fiber tested, which further reduces the average intensity coupled to the the HOM component (by a factor $\approx$1.5). Therefore, limiting to a few percent the light intensity associated to the HOM components is a reasonable assumption. Therefore, the derivation of the line-shape $I(v)$ described by Eq. (5) allows some considerations:

1. If the light intensity distribution between the pump and probe components is symmetric (Fig 8), the maximum of $I(v)$ experiences a total shift of $\Delta v_{TOT} = 0$, even in the few-mode fiber described. *Only* an asymmetric distribution between the pump/probe HOM components can cause a shift, which is incidentally the most probable situation that experimentally occurs.

2. In presence of intensity fluctuations that breaks the symmetry, since $\Gamma_0 > \Delta v_{ij}$, the maximum of the line-shape $I(v)$ can be shifted by $\Delta v_{TOT} = \pm 40$ kHz, depending on the modal content of the pump/probe beams: if only the pump beam has light in the HOM component ($f_1 = 1$, $f_2 = 0$, $f_3 = 0.99$, $f_4 = 0.01$) the shift predicted is +40 kHz, while a -40 kHz shift occurs in the opposite configuration ($f_1 = 0.99$, $f_2 = 0.01$, $f_3 = 1$, $f_4 = 0$). An oscillation (over time) between these two configurations reproduces quite well the offset frequency fluctuations presented in Figures 3 and 4 (C7$_-$ L, maximum shift observed $\pm$ 25 and $\pm$ 50 kHz, respectively).

3. A detailed analysis of the line-shape derived in Eq. (5) shows that once fixed Δn_{eff} and I_{ij}, if Γ_0 decreases the shift experienced by the maximum of $I(v)$ will decrease as well. Moreover, if $\Delta v_{ij} \geq \Gamma_0$, the HOM-FM interaction will not affect the maximum of $I(v)$, because signal generated will be far-detuned from optical transition addressed. Therefore, if the interaction between the HOM and the FM considered so far occurs in a fiber with core size larger than the C7$_-$ L one, the shift produced will be smaller compared to the one here observed/calculated. This property can explain the relative *small* shift observed in [12]: the wider core of the kagome fiber helps to reduce the total frequency shift (Δv_{TOT}), even if the Δn_{eff} between the HOMs guided in the kagome fiber (and the relative light intensity associated) could easily exceed the one considered in the calculation at point 2.

4. The frequency shift is *coupling* dependent, because a misalignment could easily increase the light intensity coupled to the HOM components. This effect is confirmed by the C19 fiber performance under temperature perturbation (Fig. 4, left): a continuous temperature variation *breaks* the modal content *symmetry*, increasing the maximum shift to $\pm$ 120 kHz.

5. The long term oscillations experienced by the C7₋PM fiber (Fig. 3, left) could also be described by the mechanism presented here, considering that the two orthogonal polarized FMs have an effective refractive index difference much smaller than the one observed for the (FM,HOM) interaction described above. A smaller effective refractive index difference will reduce the maximum theoretical shift, but the intensity coupled to the orthogonal polarized FMs could easily fluctuates over 1% due to coupling misalignment, compensating the reduction.

7. Conclusion

An optical frequency standard is developed using gas-filled single-mode HC-PCF with a core size diameter of 8 μm. A complete experimental investigation of four HC fibers is done to characterize the performances. Despite the previous recommendations, the fiber with a core diameter of only 8 μm shows a high accuracy and low fractional frequency instability (below 4×10^{-12} for averaging time between 1 s and 10^4 s). The frequency of the lock point is repeatable to ± 2.5 kHz (standard deviation over 7 measurements), resulting in the most stable and accurate laser systems locked to an acetylene filled HC fiber published so far [12, 15, 16]. This performance combined with a low temperature sensitivity and a negligible HOMs content make the C7₋S fiber a good candidate for a portable optical frequency standard. Furthermore, a simple theoretical description of the mechanism involved in the frequency shift of the locked laser is presented. The model describes the light-matter interaction with a good agreement with the experimental data, helping to select the more suitable fiber for frequency standard applications. Future investigations on the fiber crystal structure is necessary to evaluate the role of the surface modes in the energy exchange with HOMs, as well as a complete description of polarization effects.